# The Enhancement of Cold-Front Temperature Contrast by Differential Cloud Cover

M. SEGAL

*Department of Physics and Astronomy, University of Kansas, Lawrence, Kansas*

W. L. PHYSICK

*Division of Atmospheric Research, Commonwealth Scientific and Industrial Research Organisation, Victoria, Australia*

J. E. HEIM AND R. W. ARRITT

*Department of Physics and Astronomy, University of Kansas, Lawrence, Kansas*

27 May 1992 and 24 July 1992

ABSTRACT

The thermal impact of differential cloud shading across a cold front is evaluated briefly through conceptual, scaling, and numerical-modeling approaches. It is suggested that in summer the shading may enhance the boundary-layer average thermal contrast across the front by as much as 5 K for prolonged shading over the cold sector and with a dry surface in the warm sector. For short shading duration or wet surfaces along the warm sector, the thermal impact of shading reduces significantly. It is concluded that the shading effect may provide a pronounced contribution to frontogenesis for weak or moderate cold fronts.

## 1. Introduction

In a recent paper, Businger et al. (1991) suggested that "a differential cloud cover across the Piedmont front resulted in enhanced solar insolation on the warm side of the front that strengthened frontogenesis and acted further to destabilize the atmosphere." In earlier studies, Koch (1984) and Keyser (1986) also suggested enhanced frontogenesis of cold fronts due to differential cloud cover. Pinkerton (1978) reported a numerical model simulation of the effect for a specific case in which the surface sensible heat flux was prescribed. Garratt et al. (1985) provide scaling of the effect for a specific case. However, no general elaboration or quantifications were given in these studies (or appear to have been given in other studies) regarding this effect. This note provides brief scaling, numerical-modeling, and conceptual evaluations in order to assess the effect of differential cloud cover on cold-front horizontal thermal gradients. It focuses mostly on summer situations when the potential shading impact is at its peak. Some evaluations for other seasons are also provided. Scaling evaluations are given in section 2, while numerical model evaluations are provided in section 3.

*Corresponding author address:* M. Segal, Department of Physics and Astronomy, University of Kansas, Lawrence, KS 66045.

## 2. Scaling evaluations

A nonprecipitating daytime cold front over land is assumed where the cold segment C is cloudy in contrast with clear sky along the warm segment W (see Fig. 1). For scaling approximations, it is assumed that daytime surface sensible heat flux $H_s$ is linearly proportional to solar irradiance $R_s$ absorbed by the ground. Based on numerical model simulations, Segal et al. (1986) found that for clear-sky summer subtropical conditions $H_s \approx K_2(R_s - c)$, where $K_2$ is a sensible heat flux conversion factor (in these simulations $K_2 \approx 0.45$ for relatively dry surfaces and $K_2 = 0.17$ for wet surfaces), and $c \approx 100$–$200$ W m$^{-2}$. Similar relations for the midlatitudes are implied by simulations reported in Segal et al. (1989).

Assuming, for scaling purposes, the above-defined proportionality to irradiance for $H_s$, as well as uniform terrain and the absence of horizontal advection, the boundary-layer (ABL) depth $h_t$ at time $t$ can be approximated following Tennekes (1973) as

$$h_t^2 = h_{t_0}^2 + \left[ \frac{2K_1K_2(m, \theta) \int_{t_0}^{t} (K_3R_s - c)dt'}{\rho C_p \beta_0} \right], \quad (1)$$

where $h_{t_0}$ is the ABL depth at initial time $t_0$ ($t_0 = 0$ is assumed in the present scaling to be shortly following

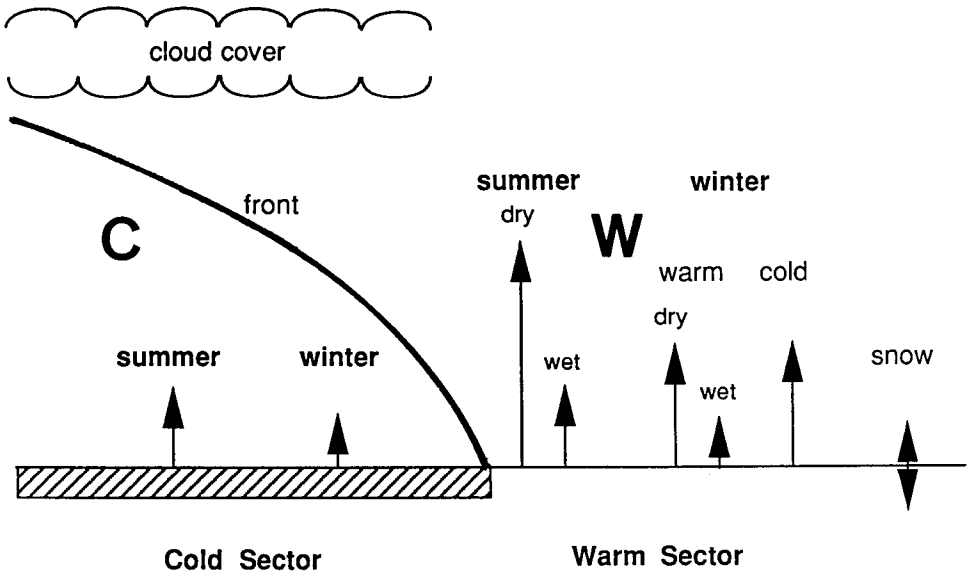


FIG. 1. Schematic illustration of cold-front transition zone and related sensible heat flux magnitude (proportional to length of arrows) over the warm sector for dry, wet, and snow-covered surface conditions. C—cold sector; W—warm sector.

sunrise; $h_{t_0} = 0$); $\rho$ and $C_p$ are the lower-atmosphere air density and specific heat, respectively; and $\beta_0$ is the potential temperature vertical gradient at time $t_0$. For the sake of simplicity, in the scaling we assume constant $\beta_0$, although generally $\beta_0 = \beta_0(z)$. The constant $K_1(\approx 1.2)$ accounts for entrainment at the ABL top. The conversion factor $K_2(m, \theta)$ is dependent on the surface moisture availability $m$ ($m = 0$ when no surface evapotranspiration exists; $m = 1$ when the surface evapotranspiration equals the potential evapotranspiration) and on the background potential temperature $\theta$ [see quantification in (iv) below]. The parameter $K_3$ indicates the fraction of solar irradiance that is absorbed by the ground compared with a situation when there is a clear sky ($K_3 = 1$ for clear sky; $K_3$ approaches 0 for thick low-level overcast).

For scaling purposes, the change of the potential temperature from its initial value, $\theta'$, is assumed to decrease linearly with height to $\theta'_h = 0$. The layer-averaged $\theta'$ within the boundary layer then is approximated by

$$\tilde{\theta}' = \frac{1}{2} h\beta_0. \qquad (2)$$

Applying Eqs. (1) and (2) over W and assuming that for bulk estimations they also can be applied over C, the difference of W − C in $\tilde{\theta}'$ due to the differential cloud cover is approximated by

$$\Delta\tilde{\theta}' = \frac{1}{2}[(h\beta_0)_W - (h\beta_0)_C]. \qquad (3)$$

Following numerical model simulations that are reported in Segal et al. (1989) for $\beta_{0_W} = 3.5$ K km$^{-1}$ (i.e., near–standard atmosphere thermal stratification shortly following sunrise) and for relatively dry-surface and clear-sky conditions during mid-August in mid-latitudes, $\tilde{\theta}'_W = 3.5$ K one hour following noon (with $h_W \approx 1500$ m). For the entire day, the integrated value of $(R_s - c)_W$ is approximately 1.7 times the corresponding value integrated to 1300 LST. Therefore, following Eqs. (1) and (2), the values of $h$ and consequently of $\tilde{\theta}'_W$ are increased by a factor of 1.3, resulting in $\tilde{\theta}'_W \approx 4.5$ K and $h_W \approx 2000$ m ($\theta'_W$ reduces about linearly from $\theta'_W \approx 9$ K near surface to $\theta'_W \approx 0$ at 2000 m). For the extreme case where $\tilde{\theta}'_C \approx 0$ (i.e., completely overcast along C), the related intensification of the thermal difference across the front in the lower atmosphere is $\Delta\tilde{\theta}' = 4.5$ K. This intensification [or its equivalent; see (ii) below] reflects in a first approximation the *maximum* possible thermal impact of differential cloud cover across a cold front when an initial standard atmosphere is assumed along the warm section. The variations in $\Delta\tilde{\theta}'$ and $h$ as $\beta_0$ changes can be estimated from Eqs. (1) and (3).

Some specific evaluations are provided:

(i) When cloud cover persists only for a portion of the day, or cloud cover is partial, the corresponding reduction in $\Delta\tilde{\theta}'$ can be estimated by adjusting $t$ and $K_3$ in Eq. (1). When cloud cover is horizontally nonuniform, further scaling assumptions should be made to consider the impact on the time-integrated surface sensible heat flux.

(ii) Increasing $\beta_0$ by a factor of $n$ (when $h_{t_0} = 0$) reduces $h$ by a factor of $n^{1/2}$, whereas $\tilde{\theta}'$ within this layer increases by $n^{1/2}$. In rigorous scaling, the height

dependence of $\beta_0$, as typical for cold fronts, should be considered.

(iii) In the winter, $\Delta\tilde{\theta}'$ is reduced compared with the summer values due to a corresponding reduction in $R_s$. (Daily clear-sky values of $R_s$ as dependent on latitude and month are available in various climatic tables.) Computations in Segal et al. (1989, Fig. 7) indicate that the midwinter $R_s$ values in midlatitude are approximately 0.3 of those in midsummer.

(iv) When the surface moisture availability $m$ is high in the warm sector (e.g., transpiring vegetation, or wet ground following previous rainfall) $H_{sw}$ is suppressed. This suppression is most pronounced when $\theta$ is relatively high. Segal et al. (1989, Fig. 6) suggest that for $\tilde{\theta} > 293$ K and $m = 0.5$, an estimation is that $K_2 \approx 0.15$ ($\tilde{\theta}' \approx 2$ K and $h \approx 1000$ m for 1300 LST mid-August solar irradiance at 40°N). When $\theta$ decreases, the Bowen ratio increases, even if the surface is saturated. For $\theta \leqslant 260$ K and $m \gtrsim 0.5$, it is estimated that $K_2 \approx 0.8$ ($\tilde{\theta}' \approx 1.5$ K and $\tilde{\theta}' \approx 2$ K at 1300 LST for mid-December and mid-February solar irradiance, respectively).

(v) Under low overcast clouds, the atmospheric longwave irradiance (LWI) that reaches the ground can be as high as 20% above clear-sky atmosphere conditions. The corresponding change in the LWI flux divergence integrated across the subcloud layer is less than 20 W m$^{-2}$ for summer conditions (e.g., Ye et al. 1989), which is about one order of magnitude smaller than $H_{sw}$. Therefore, the effect of the modified LWI on the sub–cloud layer thermal stratification is small for the purpose of the present scaling (however, it is included in the surface heat balance computations for the numerical model simulations presented in section 3). This conclusion is also supported by the cloud model simulations reported by Schmetz and Beniston (1986).

(vi) When the ground is uniformly snow covered, it can usually be assumed that, effectively, $K_2 \approx 0$, so that the differential cloud-cover effect on the front diminishes.

(vii) As pointed out by Sanders (1955), when cloudiness is diminished along C, enhanced $H_s$ values are likely to develop along C due to increased air–surface temperature contrast (compared with those along W). Simulations reported in Mahrer and Segal (1985) and Segal et al. (1989) suggested an increase as high as a factor of 0.3 in $H_s$ values due to a decrease of 10 K in the atmospheric temperature.

(viii) When precipitating fronts are considered, the evaporative cooling associated with the precipitation along C and the heating associated with condensation along the front interface provide additional diabatic forcings that affect frontogenesis. These diabatic thermal forcings may potentially be stronger than those of the cloud shading. Furthermore, unlike cloud shading, these processes produce an almost instantaneous thermal response.

## 3. Numerical model evaluations

Additional insight into the potential impact of cloud shading on cold-front horizontal thermal gradients is provided in the following through 1D and 2D numerical model simulations. In these simulations the cloud-shading effect is prescribed by reducing the incoming solar irradiance $R_S$ to the surface to $K_3 = 0.1$ of its clear-sky value. Thus, a peak shading effect is explored. The atmospheric LWI reaching the surface was increased by 0.2 compared with the clear-sky situations to account for the cloud LWI emission.

### *a. 1D numerical model simulations*

A sequence of 1D numerical model simulations using the model described in Arritt (1989) has been carried out for cloud shading initiated at 0, 1, 2 . . . 11 h after the start of integration. The simulations extended for the period 0600–1800 LST using the solar conditions at 38°N on 21 June. Standard atmosphere temperature, relative humidity of 50%, and a background geostrophic wind speed of 5 m s$^{-1}$ were prescribed as initial conditions. Two surface wetness conditions were assumed: (i) relatively dry surface with $m = 0.05$ (where $m$ is the surface moisture availability, defined as the ratio of the surface evapotranspiration to that of the potential evapotranspiration under the same surface temperature); (ii) saturated surface with $m = 1.0$. The rest of the input parameters are the same as in Physick (1988).

Figure 2 is a composite of 13 1D simulations (denoted 6–18, corresponding to the LST at which shading began) in which $\theta'$ (the change of the potential temperature from its initial value) is shown as a function of height. After shading was initiated it continued to the end of the simulation. Simulation 6 was affected by cloud shading from the commencement of the simulation at 0600 LST. The initiation of cloud shading was delayed by 1 h as the sequence number of the simulation increased. Notice that if the shading initiation time for any simulation is later than the time at which results are shown, the simulation effectively corresponds to the clear-sky case. The last simulation in the sequence (number 18) consists of clear sky throughout the whole simulation.

Figure 2a presents $\theta'$ for $m = 0.05$ at 1200 LST. At this time simulations 12–18 are identical and represent results for a clear-sky simulation commencing at 0600 LST, since the shading initiation time has not yet been reached. Simulation 6 has been affected by shading since the start of integration at 0600 LST; simulation 7 represents 1 h of clear sky followed by 5 h of shading; and so on for simulations 8–11. The near-surface $\theta'$ values in the clear-sky simulations (number 12 and larger) are larger by approximately 6 K compared with the continuous shading simulation (number 6), whereas the corresponding difference in $\theta'$ at 1000-m altitude is 3 K. These differences in $\theta'$ reduce when

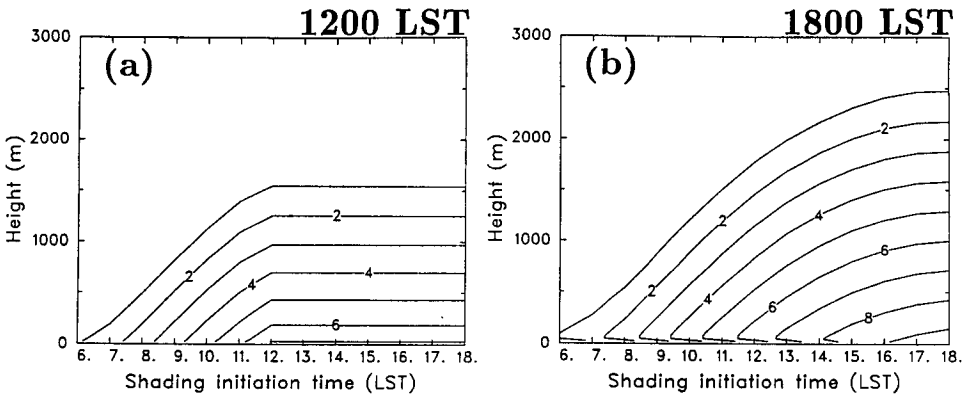


FIG. 2. A composite of $\theta'(K)$ for $m = 0.05$ based on 13 1D simulations (6–18) discussed in section 3a. The abscissa indicates the hour at which the cloud shading was initiated. (The simulation number indicates the shading initiation hour.) (a) At 1200 LST; (b) at 1800 LST.

comparison is made with simulations in which cloud shading was initiated in later hours. The noon surface sensible heat flux for the clear-sky simulations was 460 W $m^{-2}$ due to the very strong insolation and dry surface.

Figure 2b presents the simulated $\theta'$ at 1800 LST. The value of $\tilde{\theta}'$ in the clear-sky simulation (number 18) is estimated to be 5 K higher compared with the whole-day cloud-shading simulation (number 6). The corresponding difference in $\tilde{\theta}'$ reduces gradually when the shading was introduced in later hours.

Figures 3a,b are the same as Figs. 2a,b except for saturated surface conditions ($m = 1$). Similar patterns of change in $\theta'$ as a function of cloud-shading initiation hour are simulated. However, as anticipated, the values of $\tilde{\theta}'$ are reduced significantly compared with the dry surface simulations. The midday surface sensible heat flux under clear sky in these simulations was approximately 90 W $m^{-2}$.

In general the simulation results agree with the scaling in section 2. The simulations reflect two extreme summer situations in midlatitude: (i) strongly suppressed evapotranspiration (as may be typical following drought conditions, or toward the end of the summer); (ii) intense evapotranspiration as typical following precipitation events. Based on the presented results it is possible to interpolate shading impact under intermediate surface wetness conditions.

### *b. 2D numerical model simulation of cold front*

Physick (1988) suggested that differential cloud cover across cold fronts may have thermal impacts similar to those caused by differential surface heating when cold fronts move onshore during the daytime. The numerical model simulations reported in Segal et al. (1986) indicated that differential cloud cover (with $K_3 = 0.4$ in the cloudy area) resulted in $\Delta\tilde{\theta}' \approx 2.5$ K two hours after noon and induced upward vertical velocities similar to those of sea-breeze fronts. The study of Skupniewicz et al. (1991) further supports this analogy. It is therefore suggested that for "ideal" differential cloud cover across a cold front, the impact is equivalent to that of a sea-breeze circulation that is superimposed on the front (see evaluations of the latter situation in Physick 1988).

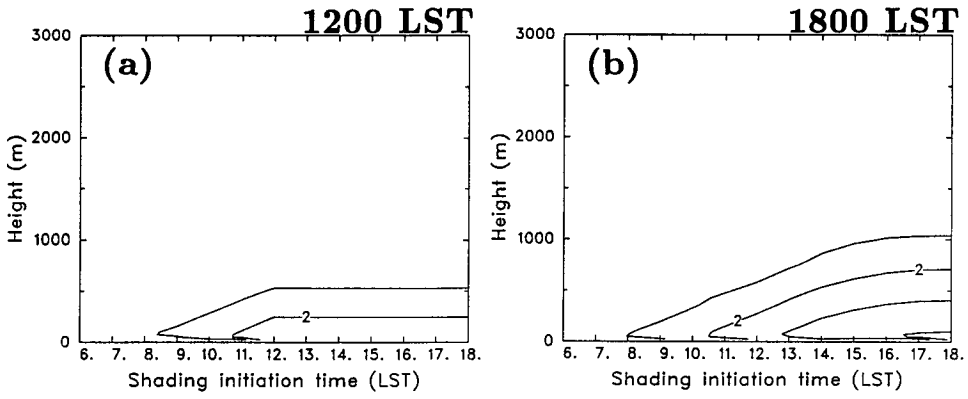


FIG. 3. The same as Fig. 2 except for $m = 1.0$.

In order to further investigate the impact of cloud shading on cold-front structure we repeated some of the cold-front simulations presented in Physick (1988) for 6 December with the following changes: (i) the entire simulated domain consisted of a land surface (with $m = 0.07$); (ii) the Southern Hemisphere conditions in Physick (1988) were converted to equivalent Northern Hemisphere conditions. Therefore, the simulated day was changed to 6 June and the Coriolis parameter sign was reversed. The model initial conditions and input parameters are the same as in Physick (1988). Clear-sky and shaded cold-front simulations were carried out. In the shaded simulation, the modification in $R_S$ and LWI (as described in the beginning of section 3) was introduced for the cloudy section of the front and followed the advance of the cold sector. The shading modifications were applied to all grid points behind the surface pressure trough.

Figures 4a and 4b present the vertical cross section of the $\theta$ field across the front at 1200 LST for clear-sky and shaded conditions. Figures 4c and 4d present the corresponding v (horizontal wind velocity) field at this hour. Comparing Figs. 4a and 4b, a noticeably sharper horizontal temperature gradient is simulated across the frontal interface in the shaded case, compared with that in the clear-sky simulation. It is interesting that the gradient farther back in the cold sector is only slightly different in both simulations (although the vertical structure of the $\theta$ field was changed in the shaded case due to the suppression of the sensible heat flux). Comparing the simulated flow fields in both simulations (Figs. 4c,d), weaker northerly flow is evident in the rear of the front interface (in the cold sector) for the clear-sky case. This is attributed to (i) stronger vertical mixing in the clear-sky case; (ii) the intensification of frontogenesis in the shaded case.

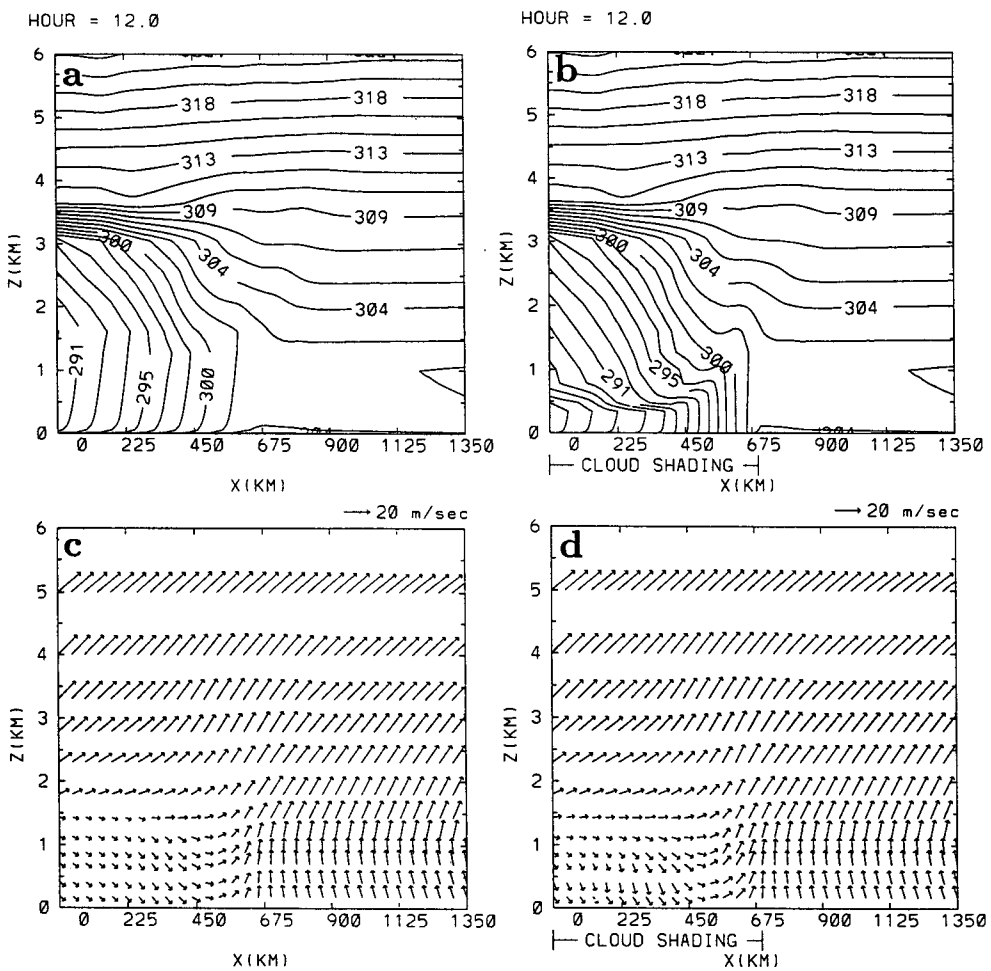


FIG. 4. Vertical cross section of the 2D cold-front simulated fields at 1200 LST. (a) The potential temperature $\theta$ (K) for the clear-sky cold-front simulation; (b) the same as (a) except for the shaded cold-front simulation; (c) the horizontal wind vector field v ($m\ s^{-1}$) for the clear-sky cold-front simulation (downward vector indicates northerly flow; rightward vector indicates westerly flow); (d) the same as (c) except for the shaded cold-front simulation.

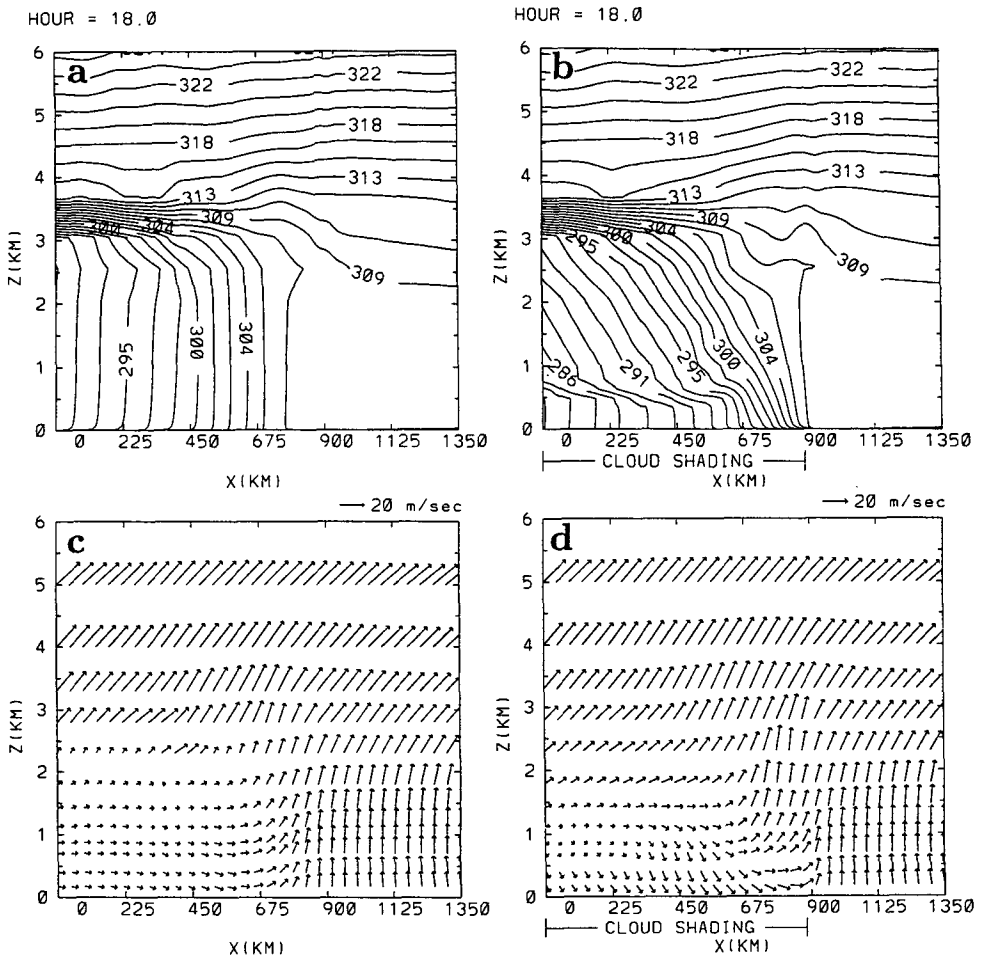


FIG. 5. The same as in Fig. 4 except for 1800 LST.

Figure 5 presents the $\theta$ and v fields as in Fig. 4 except for 1800 LST. The bunching of the isotherms at the leading edge of the cloud-shaded front is still pronounced, although they are now beginning to slope backward due to vertical wind shear and the decay of convective mixing. In a similar manner to that described in Physick (1988) for cold fronts crossing coastlines, the shaded frontal system at 1800 LST is behaving as a gravity current inasmuch as there is a region of cold air at low levels moving faster than the front. One consequence of this may be seen in the wind field (Fig. 5d) where a shallow nose appears to have developed at the leading edge of the original front. It is also obvious by 1800 LST that the shaded front travels faster than a front without cloud shading. Tower measurements analyzed by Shapiro (1984) indicated that a well-developed cold front had a structure similar to an advancing gravity current. This was confirmed by Shapiro et al. (1985), who also found that the strong vertical velocities at the front–gravity-current head could provide a mechanism for the release of potential instability.

Finally, we note that the simulations presented in this subsection (almost peak solar irradiance for midlatitudes; relatively dry surface conditions) provide an example for peak potential impact of cloud shading on frontogenesis in midlatitudes. We expect that this impact is likely to be most pronounced when weak to moderate cold fronts are considered.

## 4. Conclusions

The potential impact of daytime differential cloud cover across cold fronts on frontogenesis has been briefly evaluated. Differential cloud cover may contribute in extreme situations (i.e., midlatitude summer conditions; continuous overcast in the cold section; dry land surface) to average increases of approximately 5 K in the boundary-layer temperature difference across the cold-front interface. This occurs within the layer of typical ABL depth of approximately 2000 m when standard atmosphere stratification in the front warm sector is assumed around sunrise. Therefore, we suggest that the effect on frontogenesis should be most notice-

able for relatively weak fronts. In situations associated with partial or short-duration cloud cover, the relative reduction in the aforementioned thermal effect can be scaled easily based on approximations outlined in Eqs. (1) and (2). For some surface conditions (including very wet surface in the summer, or snow-covered ground) the diabatic frontogenesis effect due to differential cloud cover can be practically ignored.

Two-dimensional numerical simulations have suggested two further effects of cloud shading across a front, namely, (i) the acceleration of the front compared to the clear-sky case, and (ii) the development of a shallow gravity-current–type nose at the leading edge of the front.

*Acknowledgments.* The study was supported in part by NSF Grant ATM-9114736. Reta Solwa prepared the manuscript.

## REFERENCES

Arritt, R. W., 1989: Numerical modeling of the offshore extent of sea breezes. *Quart. J. Roy. Meteor. Soc.*, **115,** 547–570.

Businger, S., W. H. Bauman, III, and G. F. Watson, 1991: The development of the Piedmont front and associated outbreak of severe weather on 13 March 1986. *Mon. Wea. Rev.*, **119,** 2224–2251.

Garratt, J. R., W. L. Physick, R. K. Smith, and A. J. Troup, 1985: The Australian summertime cool change: Mesoscale aspects. *Mon. Wea. Rev.*, **113,** 202–223.

Keyser, D., 1986: Atmospheric fronts: An observational perspective. *Mesoscale Meteorology and Forecasting,* P. S. Ray, Ed., Amer. Meteor. Soc., 216–258.

Koch, S. E., 1984: The role of an apparent mesoscale frontogenetic circulation in squall line initiation. *Mon. Wea. Rev.*, **112,** 2090–2111.

Mahrer, Y., and M. Segal, 1985: Model evaluations of the impact of perturbed weather conditions on soil-related characteristics. *Soil Science,* **140,** 368–375.

Physick, W. L., 1988: Mesoscale modeling of a cold front and its interaction with diurnally heated land mass. *J. Atmos. Sci.*, **45,** 3169–3187.

Pinkerton, J. E., 1978: Numerical experiments on boundary layer effects on frontal structure. Ph.D. dissertation, 215 pp. [Available from the University Microfilms International, Ann Arbor, Michigan.]

Sanders, F., 1955: An investigation of the structure and dynamics of an intense surface frontal zone. *J. Meteor.*, **12,** 542–552.

Segal, M., F. W. Purdom, J. L. Song, R. A. Pielke, and Y. Mahrer, 1986: Evaluation of cloud shading effects on the generation and modification of mesoscale circulations. *Mon. Wea. Rev.*, **114,** 1201–1212.

——, J. R. Garratt, G. Kallos, and R. A. Pielke, 1989: The impact of wet soil and canopy temperatures on daytime boundary layer growth. *J. Atmos. Sci.*, **46,** 3673–3684.

Schmetz, J., and M. Beniston, 1986: Relative effects of solar and infrared radiative forcing on mesoscale model. *Bound.-Layer. Meteor.*, **34,** 137–155.

Shapiro, M. A., 1984: Meteorological tower measurements of a surface cold front. *Mon. Wea. Rev.*, **112,** 1634–1639.

——, T. Hampfel, D. Rotzoll, and F. Mosher, 1985: The frontal hydraulic head: A micro-$\alpha$ scale ($\sim$1 km) triggering mechanism for mesoconvective weather systems. *Mon. Wea. Rev.*, **113,** 1166–1183.

Skupniewicz, C. E., J. W. Glendening, and R. F. Kamada, 1991: Boundary-layer transition across a stratocumulus cloud edge in coastal zone. *Mon. Wea. Rev.*, **119,** 2337–2357.

Tennekes, H., 1973: A model for the dynamics of inversion above a convective boundary boundary-layer. *J. Atmos. Sci.*, **30,** 558–567.

Ye, Z. J., M. Segal, J. R. Garratt, and R. A. Pielke, 1989: On the impact of cloudiness on the characteristics of nocturnal downslope flows. *Bound.-Layer. Meteor.*, **49,** 23–51.